Supporting Information

for

Band–Like Transport of Charge Carriers in Oriented Two–Dimensional Conjugated Covalent Organic Frameworks

Samrat Ghosh[1,2],* Yusuke Tsutsui[1],* Takahiro Kawaguchi[1], Wakana Matsuda[1], Shusaku Nagano[3], Katsuaki Suzuki[4], Hironori Kaji[4], and Shu Seki[1]*

[1]Department of Molecular Engineering, Graduate School of Engineering, Kyoto University, Nishikyo–ku, Kyoto 615–8510, Japan.
[2]Inorganic and Physical Chemistry Laboratory, CSIR–Central Leather Research Institute, Chennai–600020, India.
[3]Department of Chemistry, College of Science, Rikkyo University, 3–34–1 Nishi–Ikebukuro Toshima–ku, Tokyo 171–8501, Japan.
[4]Institute for Chemical Research, Kyoto University, Uji, Kyoto, 611–0011, Japan.

General: All the starting materials, reagents and solvents for the syntheses were purchased from Tokyo Chemical Industry (TCI), Wako, Sigma Aldrich or AGC and used without any further purification. The respective aldehyde and amine functionalized ligands were synthesized and purified following previous literature reports and modified accordingly to improve the yields.

Characterization: Solution state ^{1}H and ^{13}C NMR spectra were obtained in chloroform–*d* ($CDCl_3$), and acetone–d_6 using TMS (0 ppm for ^{1}H) or $CDCl_3$ (77 ppm for ^{13}C) as an internal standard, recorded on a JEOL JNM–AL400 FT–NMR (^{1}H: 400 MHz; ^{13}C: 100 MHz) spectrometer. Solid–state magic angle spinning (MAS) ^{13}C NMR measurements were performed using a Bruker Advance III 400 MHz spectrometer operating under a static field of 9.4 T. A triple resonance probe with a 4.0 mm MAS probe head was used. For cross polarization (CP) MAS experiments, ^{1}H and ^{13}C field strengths of 55.6 kHz were used for the CP process, and the contact time was 2 ms. SPINAL 64 ^{1}H dipolar decoupling with a ^{1}H field strength of 100 kHz was applied during the detection of free induction decay. The dipolar dephasing MAS spectra, which selectively provide the resonance lines of quaternary carbons, were measured

with a $^{1}H–^{13}C$ dipolar dephasing time of 1.8 ms and a 180° pulse was applied in the middle of the dephasing time. The ^{13}C chemical shifts were expressed as values relative to tetramethylsilane using the $–CH_2$ resonance peak at 38.3 ppm for adamantane as an external reference. The MAS spinning speed was set to 12 kHz and the experiments were conducted at 300 K. The –CH carbon spectra were obtained by subtracting quaternary carbon spectra from all carbon spectra.

Fourier–Transform Infrared (FT–IR) spectra were recorded on a JASCO FT–IR 4700 instrument. Solid COF samples were directly placed in germanium cell and attenuated total reflectance (ATR) were measured for 512 scans. Raman spectra of all the COFs were recorded on a JASCO NRS–4100, Confocal Raman Microscope. Solid COF samples (as pallet) or films were placed over quartz substrates and 532 nm laser was used and averaged with 1024 scans. Powder X–ray diffraction (PXRD) measurements were carried out using a Rigaku MiniFlex 600 (Bragg–Brentano geometry, Cu Kα radiation λ = 1.54 Å) instrument with X–ray tube voltage of 40 kV and the current of 15 mA. Solid samples were placed uniformly over a glass sample holder and data were collected in reflection mode with a scan speed of 1 degree/ minute. Background correction was performed using the empty sample holder and subtracted from the sample. To identify the molecular orientation in the COF film, a 2D grazing–incidence X–ray scattering (2D–GIXS) measurement was performed using a Rigaku FR–E/R–AXIS IV system with a GI sample stage at the X–ray tube voltage of 45 kV and the current of 45 mA. The distance between the sample film and the R–AXIS IV (2D detector) was 300 mm. CuKα radiation (λ = 1.54 Å) was utilized as the incident X–ray for the measurements. Adsorption isotherms of N_2 at 77 K were measured with Bellsorp–mini Ⅱ equipment. Before the adsorption measurements, powdered samples were activated under reduced pressure ($<10^{-5}$ bar) at 120 °C for 12 h. For the evaluation of the surface area, the BET model was applied in the ranges $0.05 \leq p/p_0 \leq 0.25$.

Spectrometry: Absorption spectra of the COF films were recorded on a JASCO V–570 UV–Vis–NIR spectrophotometer from 300 to 800 nm at ambient atmosphere. The COF films were directly grown or placed over a quartz substrate and absorption spectra was measured in transmission mode with a resolution bandwidth was set as 1 nm with the scan rate of 1000 nm/min. Fluorescence spectra of the COF films were measured on a JASCO FP–8500 fluorescence spectrophotometer. Right angle fluorescence spectra were collected for both of **AntTTH** and **AntTTF** film having an average thickness of ~570 and ~200 nm respectively. Both the films were excited at 475 nm where the optical density of **AntTTH** is 5–fold higher

than **AntTTF**, however still **AntTTF** exhibited ~8 fold enhanced photoluminescence. Photoelectron Yield Spectroscopy (PYS) measurements were carried out by pasting COF powders over conductive carbon tape–coated glass plate and placed in a Bunko Keiki BIP–KV202GD instrument. Photocurrent responses were collected under a range of light illumination (hν = 4 ~ 7.5 eV). The ionization energy was estimated using the cross section of [photoelectron yield]$^{1/3}$ as a function of hν. The valence band was calculated from the onset energy.

Morphological Traces: Morphological analyses of the COFs were performed using a JEOL JSM–7001F scanning electron microscope (SEM) with acceleration voltage of 15.0 kV. COF films were placed over clean silicon wafer and imaged under high vacuum. Low temperature high–resolution transmission electron microscope (cryo–TEM) were performed for the powder and film samples of COF, placed over carbon coated copper grid and imaged using JEOL JEM–2100F(G5) TEM. Atomic Force Microscopy images were recorded under ambient conditions using a Multimode AFM (Bruker Co.) operating with a tapping mode regime.

Structural Modeling and Band Structure Calculation: Molecular modeling of the COFs was performed using Materials Studio (2018) software package.[1] Firstly, smallest repeating unit of the COF was placed in a crystal cell with P1 symmetry and geometric optimizations were performed using self−consistent−charge (SCC) density functional tight binding method (DFBT+).[2−5] Geometrical optimization was performed using smart algorithm, which is a cascade of the steepest descent, ABNR (adjusted basis set Newton−Raphson), and quasi−Newton methods. Universal force field (UFF)−based Lennard−Jones dispersion corrections was used for the calculation.[6,7] The 3ob parameters was used from the Slater−Koster library and SCC convergence tolerance set at 1 x 10^{-8}.[8] Divide and conquer was used as the eigensolver. For both the COFs, AA and AB stacks were considered by creating corresponding unit cells and their geometry were optimized, followed by the imposition of high symmetry. Simulated powder diffraction patterns and refinements of PXRD pattern were calculated using Reflex module of Material studio.

Energy optimization was performed using DMol3 in Materials Studio using exchange-correlation potential, described by generalized gradient approximation (GGA) in the form of Perdew−Burke−Ernzerhof (PBE) function using Grimme method for DFT–D correction.[9−12] For electronic calculations, SCF tolerance was kept 10^{-6} and it converged. All electron relativistic core treatment was performed, that includes scalar relativistic effects

(pseudopotential vpsr) using Double Numerical plus polarization (DNP) basis set (basis version 4.4).[13] The global orbital cutoff set as 3.7 Å. Monkhorst–Pack grid parameter for the k–point sampling of the Brillouin zone was set to be 6×6×1. Electronic band structures and corresponding density of sates (DOS) were calculated for single layer and 5–layers of COFs using at k–point. HOMO and LUMO were calculated at Γ–point.

The density functional theory (DFT) calculations for the small repeating units were carried out using B3LYP function and 6−31g* as the basis in the Gaussian09 suite (Revision D.01).[14]

Photoconductivity Measurements: Photoconductivity transients, demodulated through a GaAs crystal–diode with Schottky–barriers (rise time < 1 ns), were monitored by a Tektronix model TDS3032B digital oscilloscope. Time constant (τ) of the present TRMC system was then determined by the Q–value of microwave cavity (Q = 2000), leading to $\tau = \frac{Q}{2f} \sim 100\ ns$. The observed conductivities were normalized, given by a photocarrier generation yield (φ) multiplied by sum of the carrier mobilities of electron/hole ($\Sigma\mu$), according to the equation,

$$\varphi\Sigma\mu = A\Delta P_R / eI_0 F_L P_R$$

where, e, A, I_0, F_L, P_R, and ΔP_R are elementary charge, sensitivity factor (S cm^{-1}), incident photon density of the excitation laser (photon cm^{-2}), correction factor (cm^{-1}) for overlapping between special distribution of photo–generated charge carriers and electromagnetic field strength of probing microwave in the cavity, and reflected microwave power and its transient change, respectively.

Temperature dependent photoconductivity was measured by fixing the sample inside a hollow quartz tube and placed inside the microwave cavity. Nitrogen (N_2) gas was cooled by flowing through copper tube immersed in liquid N_2 and connected to the one side of the quartz tube. Temperature was controlled by controlling the flow rate of cooled N_2 and photoconductivity measurements was performed from 190 K to 298 K. Schematic of the experimental set–up is given below.

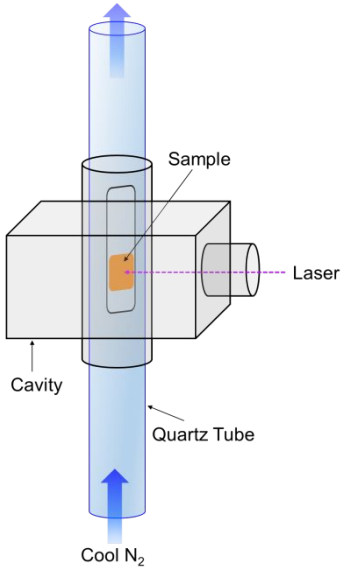

The FP–TRMC measurements were performed for COF films and powders over quartz substrate. COF films or powders were transferred over the quartz substrate and coat with CYTOP polymer (insulating polymer) for fixing.

The spatial size (Δx) of statistical local motion of charge carriers is estimated during turn–over period of electric field of the probing 9.1 GHz microwave by the following Kubo equation.

$$\Delta x = \left(\mu k_B T f^{-1} e^{-1}\right)^{1/2}$$

where μ, k_B, f, and e are charge carrier mobility, Boltzmann's constant, frequency of microwave, and elementary charge, respectively. Generally, Δx corresponds to the crystalline domain size of the semiconductor. Hence, based on Kubo equation, increase in charge carrier mobility can be expected with the increase in crystalline domain size.

Synthesis of the building blocks:

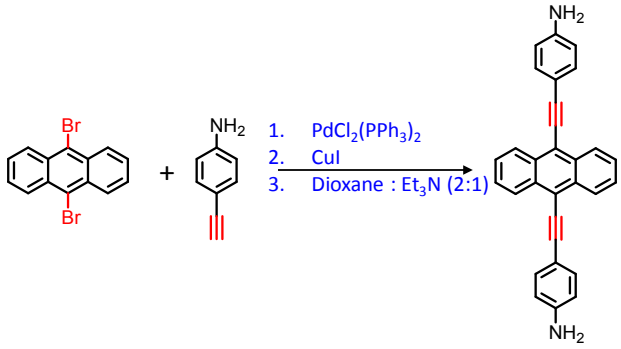

Synthesis of 9,10–bis(4–aminophenylethynyl) anthracene (AntT):

A mixture of 9,10–dibromoanthracene (1 g, 2.97 mmol, 1 equiv), 4–Ethynylaniline (870 mg, 7.43 mmol, 2.5 equiv), Bis(triphenylphosphine)palladium chloride ($PdCl_2(PPh_3)_2$, 100 mg, 0.14 mmol, 0.05 equiv) and Copper(I) iodide (CuI, 60 mg, 0.3 mmol, 0.1 equiv) was taken in a two–neck round bottom flask charged with magnetic stir bar and fitted with a condenser and placed under inert atmosphere. In that mixture 30 mL dry Dioxane was added and immediately freeze–pump–thaw in liquid nitrogen to remove oxygen from the reaction mixture. Subsequently, 10 mL triethylamine was added to the reaction mixture and repeated the freeze–pump–thaw process for 15 minutes. After that, the reaction mixture was allowed to come to room temperature and heated at 80°C for 48 h under inert atmosphere. The reaction color changed from light yellow to dark red with the progression of the reaction. After completion of the reaction, dioxane and triethylamine was removed in rotary evaporator under reduced pressure. The residue was purified by column chromatography using amine functionalized SiO_2 (metal ion scavenger) and eluted with chloroform/acetone (95:5). The product was recrystallized from acetone/dichloromethane/hexane to obtain shining red crystals. Yield: 700 mg (~60 %). ^{1}H–NMR (400 MHz, acetone–*d*6, δ): 8.73 (m, 4H), 7.71 (m, 4H), 7.58 (d, 4H), 6.80 (d, 4H), 5.22 (s, 4H). MS (ESI): 408.7; Exact Mass: 408.5.

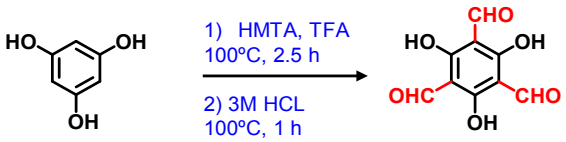

Synthesis of 2,4,6–trihydroxybenzene–1,3,5–tricarbaldehyde (TH):

To a mixture of hexamethylenetetraamine (15 g, 108 mmol) and phloroglucinol (6 g, 49 mmol), 90 mL trifluoroacetic acid was added under N_2. The mixture was heated at 100 ºC for 3 h followed by addition of 150 mL 3 M HCl. The solution was again heated at 100 ºC for 1 h. After cooling to room temperature, the solution was filtered through celite, extracted with dichloromethane and dried over magnesium sulfate. Solvent was removed under reduced pressure to give an off–white powder which was then purified by column chromatography on silica gel using acetone and dichloromethane (2:1) as eluent. Yield: 1 g (10%). ^{1}H–NMR (400 MHz, chloroform–*d*, δ): 14.06 (s, 3H), 10.09 (s, 3H). ^{13}C–NMR (100 MHz, chloroform–*d*, δ): 192.0, 173.6, 102.9. HRMS: 211.1019 $[M+H]^{+}$; Exact Mass: 210.02.

Additional Figures

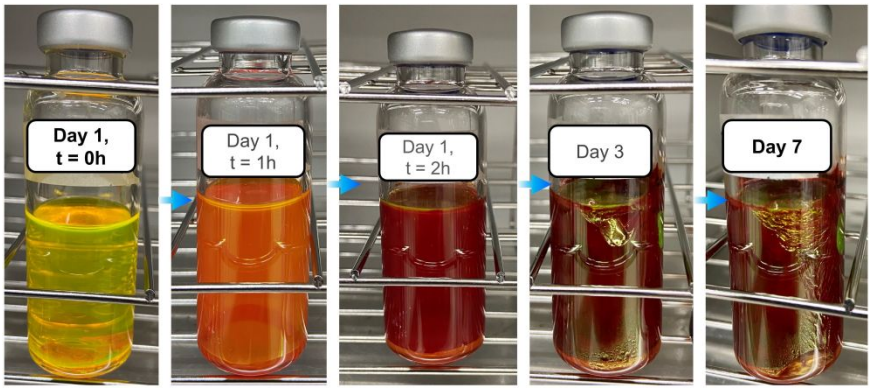

Figure S1. Photographs showing the synthesis of **AntTTH** film at different time interval, under ambient light inside oven at 120 °C. The color change and film formation on the wall of the reaction tube with the progression of reaction are clearly visible.

Regarding the size of COF film synthesis, the COF films were grown on the wall the of the reaction tube and hence its size depends on the reaction tube. The diameter of the tube is 2 cm, therefore the circumference is 6.28 cm and height is ~5 cm (Figure 1), hence approximately 2×2 inch COF films can be grown. Principally, larger size COF films can be prepared by increasing the reaction tube diameter and solvent height. However, these COF films are delicate and hence difficult to remove and place over desired substrate as a monolith.

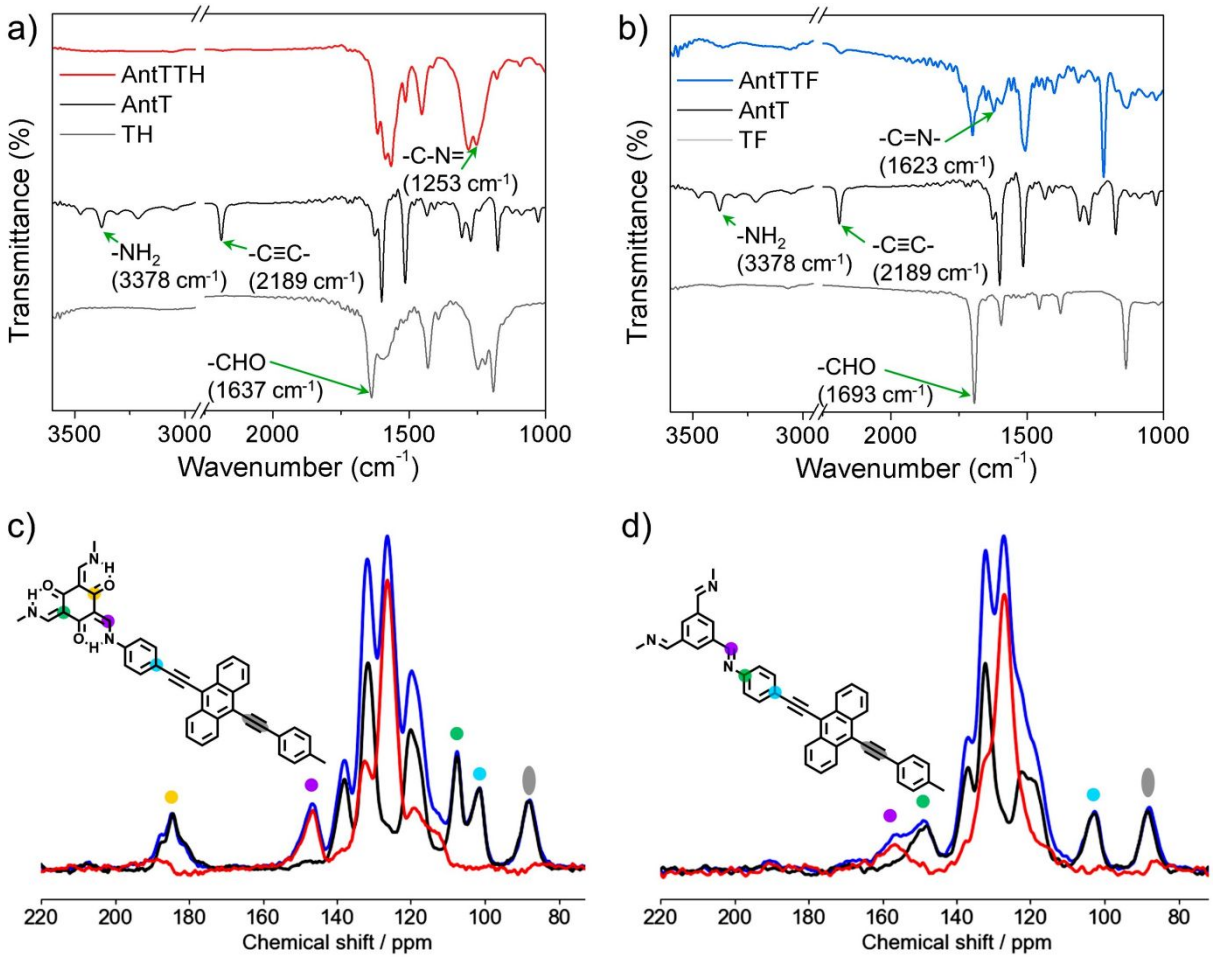

Figure S2. FT–IR spectra of a) **AntTTH** and b) **AntTTF** along with their corresponding building blocks. ^{13}C CP/MAS spectra of all carbons (blue line), quaternary carbons (black line) and –CH carbons (red lines) of c) **AntTTH** and d) **AntTTF**.

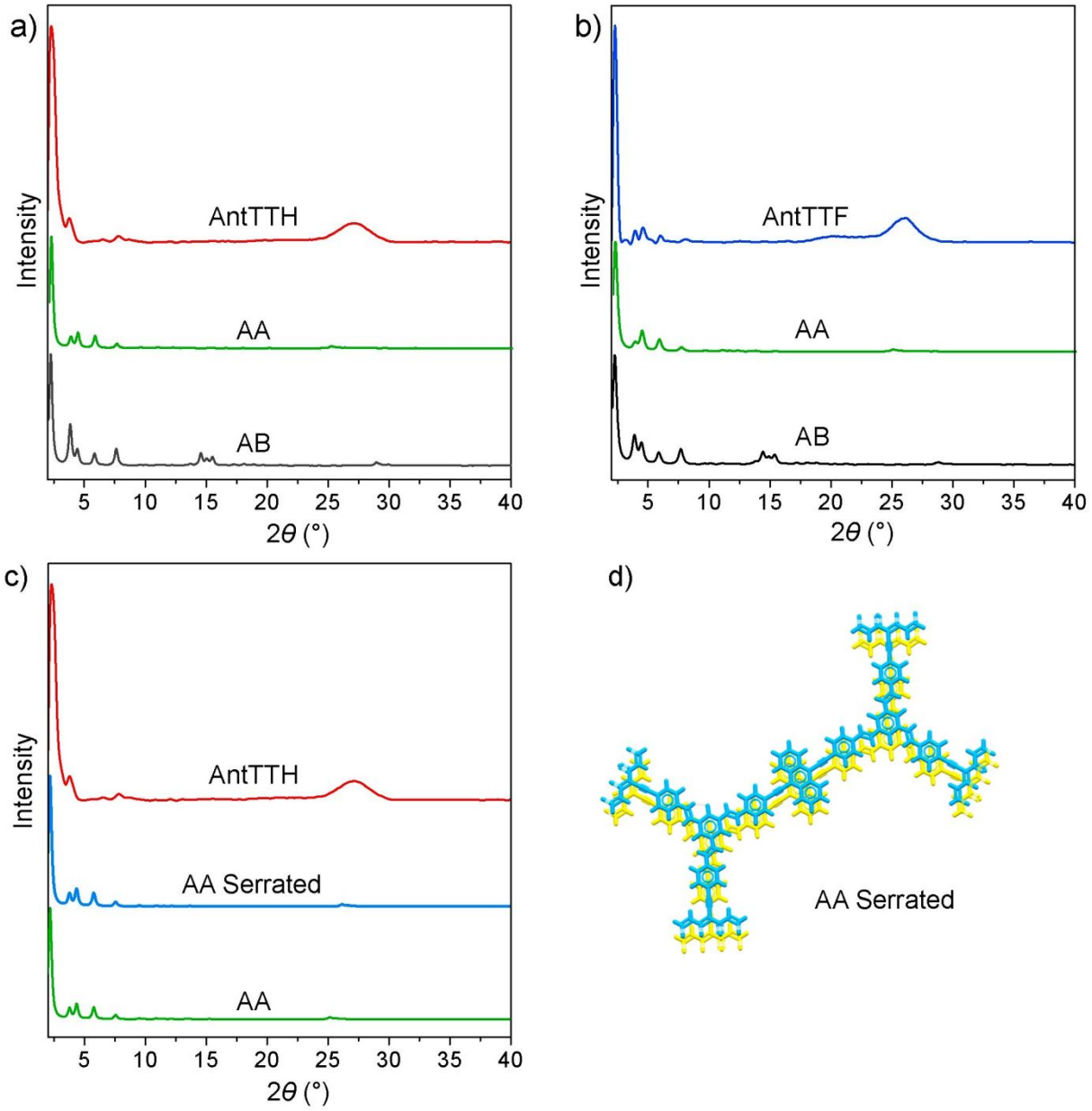

Figure S3. Experimental PXRD of a) **AntTTH**, and b) **AntTTF**, with simulated PXRD pattern. c) Comparison of PXRD between experimental (red), serrated (~1 Å) AA (cyan) and AA (green) structure of **AntTTH**. d) Schematic representation of a serrated AA structure.

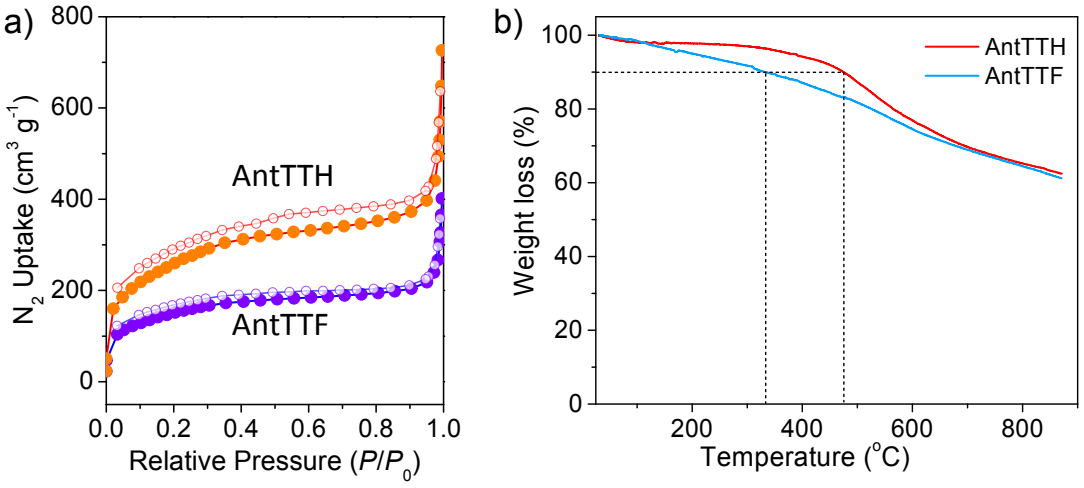

Figure S4. a) Nitrogen sorption isotherms at 77 K for **AntTTH** (orange)and **AntTTF** (violet). b) TGA profiles of **AntTTH** (red) and **AntTTF** (blue) and dotted line indicates the 10% decomposition temperature.

Thermal gravimetric analysis (TGA) analysis revealed that **AntTTF** and **AntTTH** exhibited 10% decomposition at 325 and 470°C respectively, thereby confirming the enhanced chemical stability of **AntTTH**.

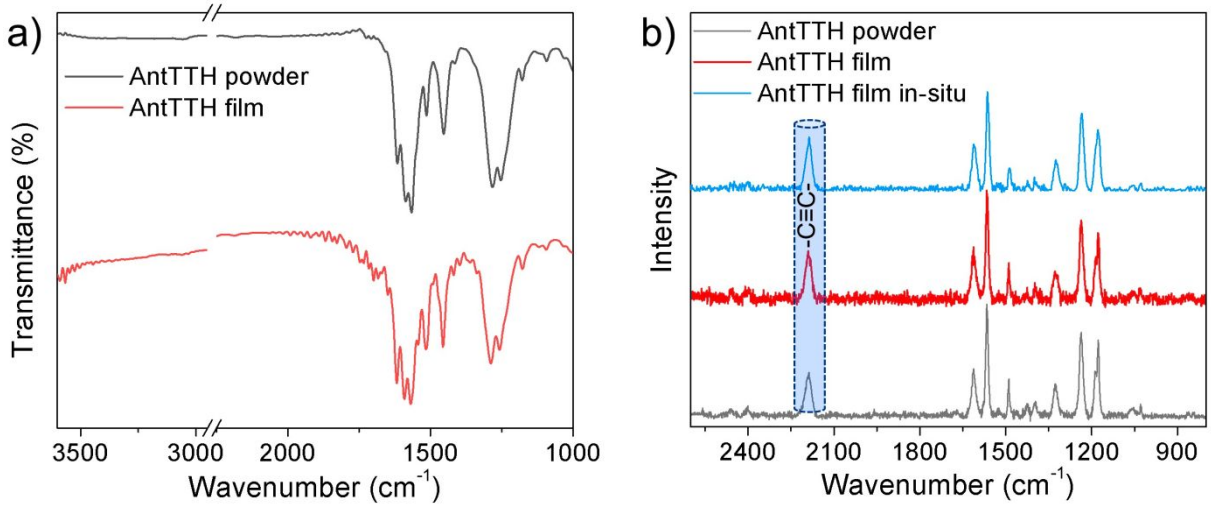

Figure S5. a) FT–IR of powder and film of **AntTTH** and b) Raman spectra of powder, transferable film and in–situ grown film of **AntTTH**.

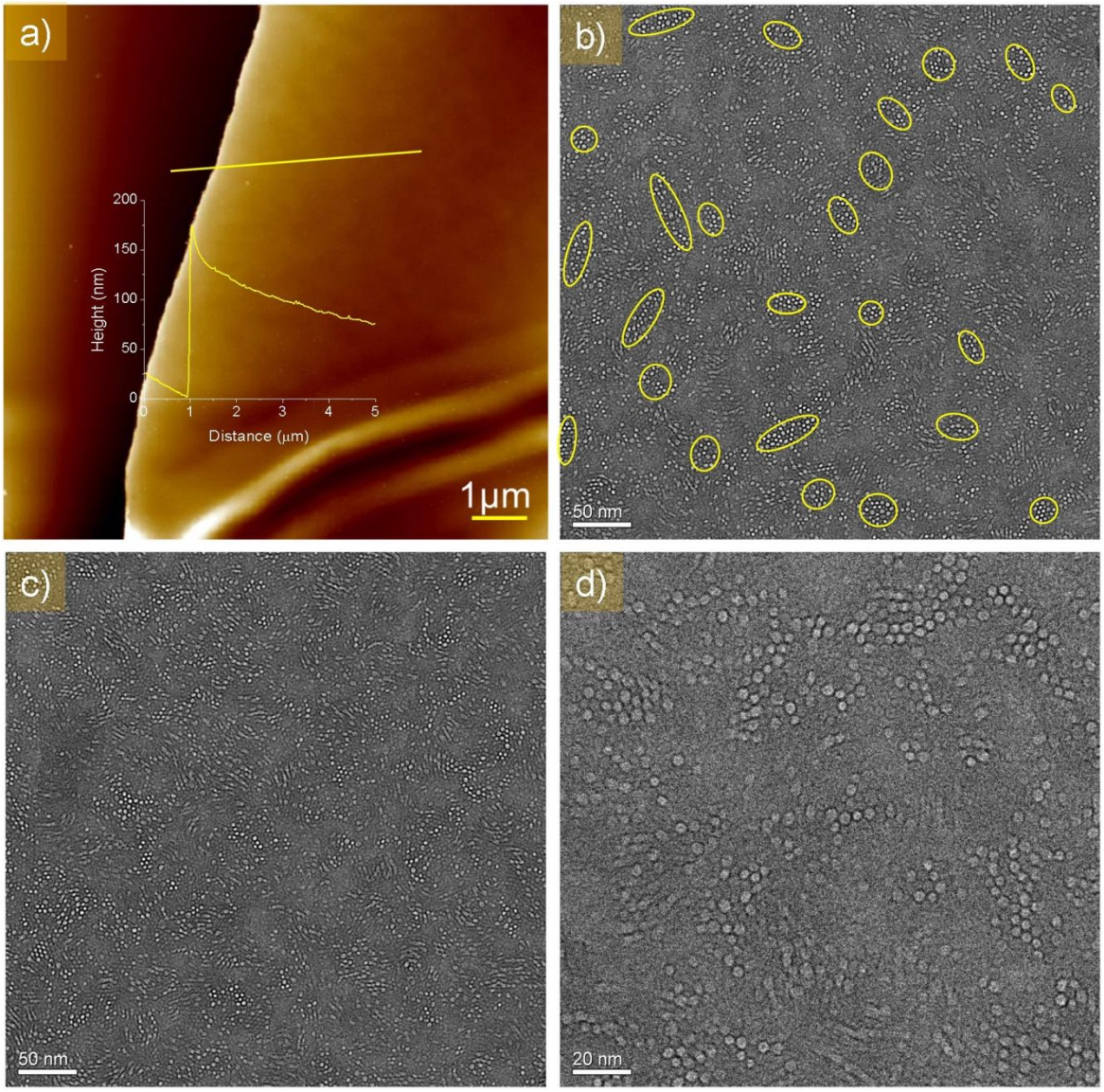

Figure S6. a) AFM image of **AntTTH** film with corresponding height profile as inset. b–d) High resolution cryo–TEM images of **AntTTH** film, yellow circles represent the crystalline domain with the repeating honeycomb framework.

In the TEM images (Figure 6b–d), large section looks crystalline with lattice fringes. Some of the honeycomb lattices are focused, whereas others are slightly unfocused and it can be reversed upon adjusting the focus. This focusing issue was encountered during the high–resolution cryo–TEM measurement and it was difficult to focus different areas simultaneously, probably due to the wiggling nature of COF film. As a result, it is difficult to identify and quantify the amorphous domains in the COF film.

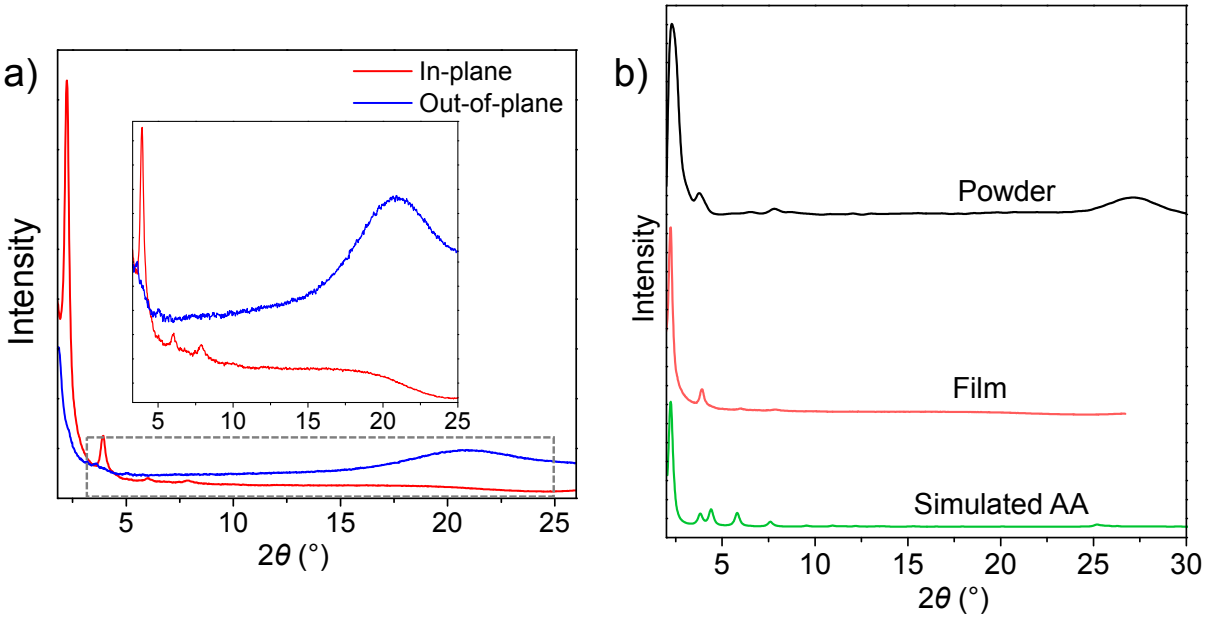

Figure S7. a) 1D plot of GIXS showing in–plane and out–of–plane profiles for the optimized structures of **AntTTH** film. b) Experimental PXRD of **AntTTH** powder, in–plane profile of **AntTTH** film and its simulated PXRD pattern.

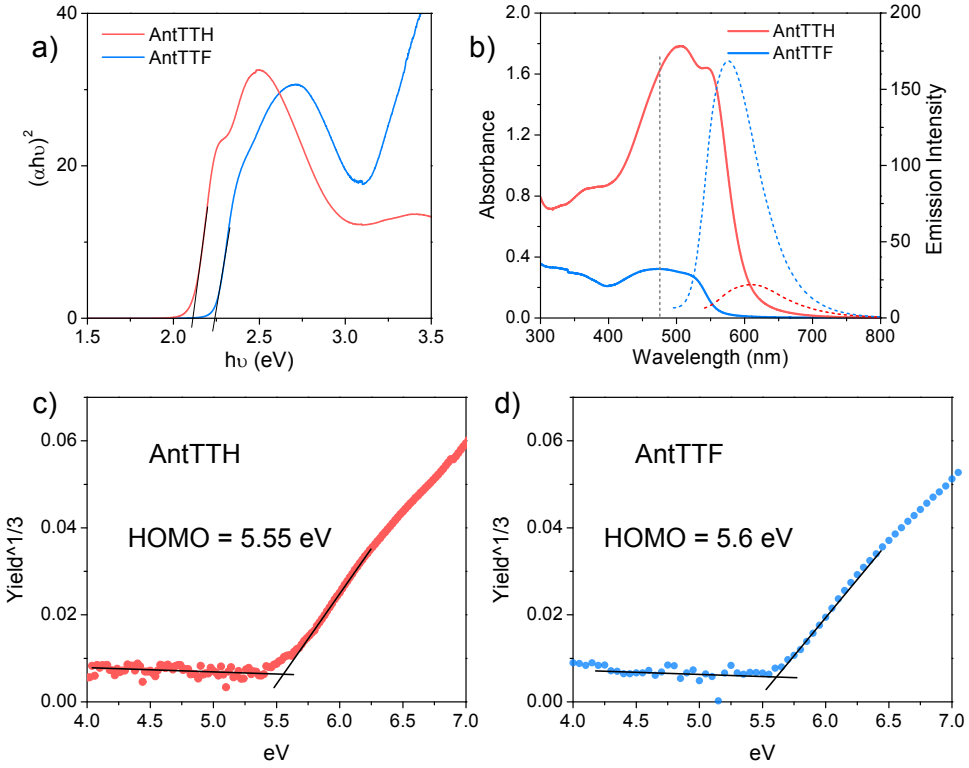

Figure S8. a) Tauc Plot of **AntTTH** and **AntTTF**. b) Steady–state absorption and emission spectra of **AntTTH** (red) and **AntTTF** (blue) films with the excitation at 475 nm. Photo yield spectra (PYS) of c) **AntTTH** and d) **AntTTF** with corresponding HOMO energy level.

Figure 8b shows the absorption and photoluminescence (right angle fluorescence) spectra of **AntTTH** and **AntTTF** film having an average thickness of ~570 and ~200 nm respectively, measured under identical conditions. Both the films were excited at 475 nm where the optical density of **AntTTH** is five–fold higher than **AntTTF**, however, **AntTTF** exhibited ~8 fold enhanced photoluminescence. Upon normalizing the absorption, the emission intensity of **AntTTF** was found to be ~40 fold higher than the **AntTTH**. Our attempt to calculate the photoluminescence quantum yield (QY) failed because of very low QY and it comes in the error limit of the integrated sphere method.

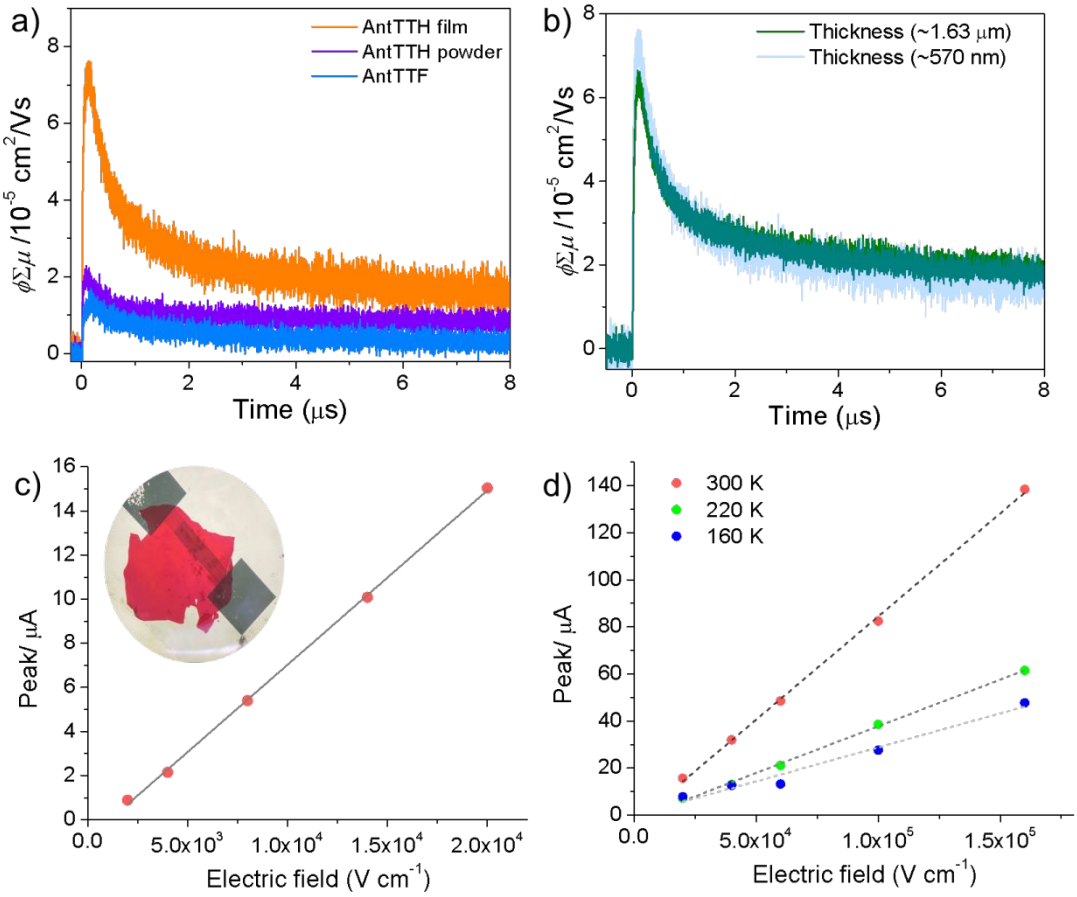

Figure S9. FP–TRMC photoconductivity transient of a) **AntTTH** COF film, powder and **AntTTF** and b) **AntTTH** COF film with different thickness. Peak of transient photocurrent intensity *vs* electric field plot of **AntTTH** COF film at c) room temperature (under low electric field) and d) at 300, 220 and 160 K (under high electric field), showing linear relation. All the experiments were performed under 355 nm laser excitation with 9.1×10^{15} photons cm^{-2}pulse^{-1}.

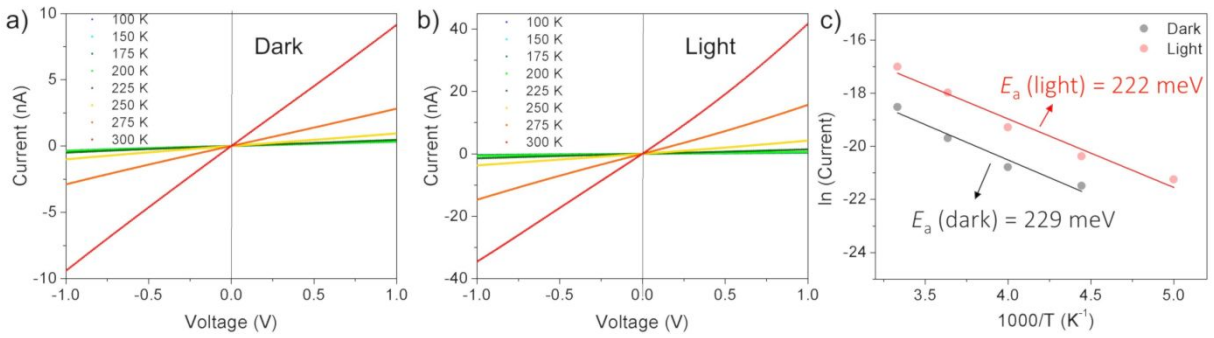

Figure S10. *I–V* characteristics of **AntTTH** film measured under a) dark and b) light at temperatures ranging from 100 K–300 K. c) Arrhenius plot of current in dark and light.

The present COF is highly sensitive to the external light (even to the room light), that the photogenerated charges can behave as trapped charge carriers which has long lifetime more than minutes. For example, dark current is stable during the measurement, but it reduces dramatically after application of high voltage between source and drain, clearly indicating that long–lifetime trapped carriers are extracted due to high electric field via Poole–Frenkel mechanism. Besides, the current–temperature plot taken from *I–V* measurement slightly deviates from straight line as shown in Figure S10c, which shows the trend that larger current than expected from single Arrhenius relation in both light and dark conditions. This indicates that the macroscopic measurement contains multiple trap–and–release model.

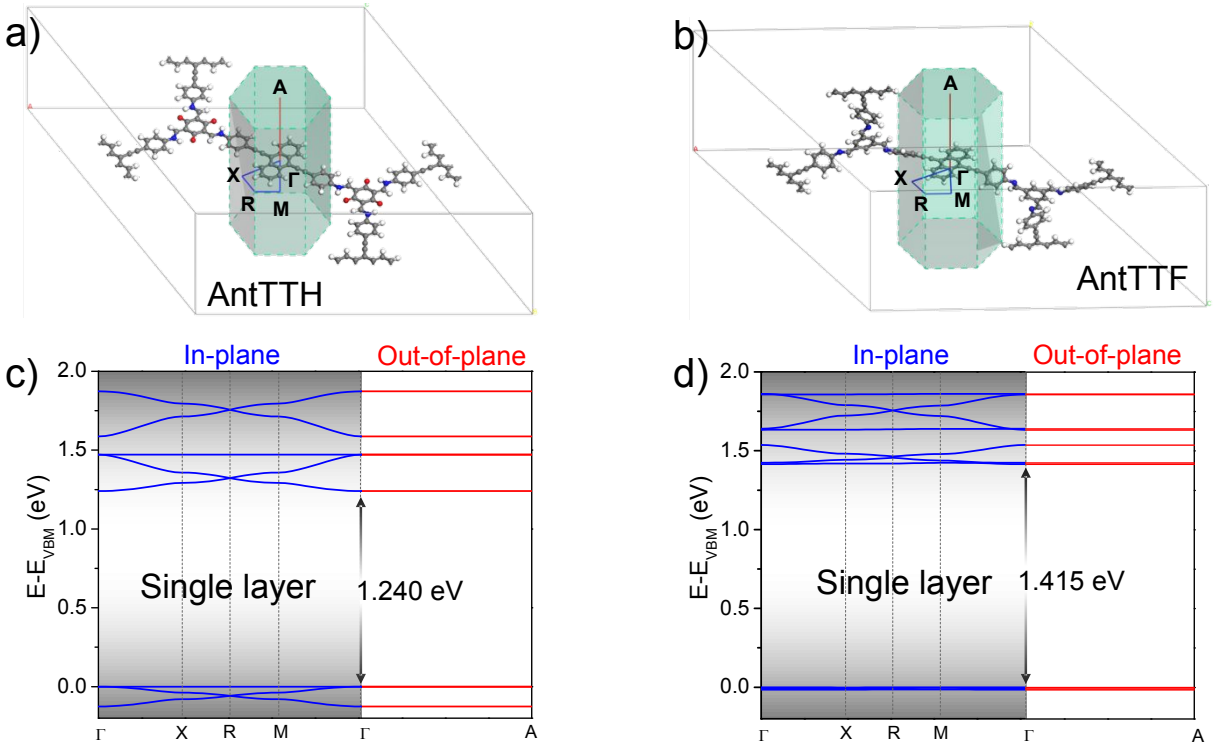

Figure S11. The first Brillouin zone of a) **AntTTH** and b) **AntTTF**. Calculated electronic band structure of single layer and AA stacked five layer of c) **AntTTH** and d) **AntTTF** with the corresponding band gaps.

The single layer of **AntTTH** was modeled by adding a vacuum space of 20 Å along *c*–axis to avoid any interaction between layers. To understand the effect of stacking, the band structures was calculated for 5 layers of AA stacked **AntTTH**, where interlayer distance is 3.547 Å. Upon increasing the number of layers, in–plane band structure and band gap changed significantly, however out–of–plane band structure still remained dispersion less.

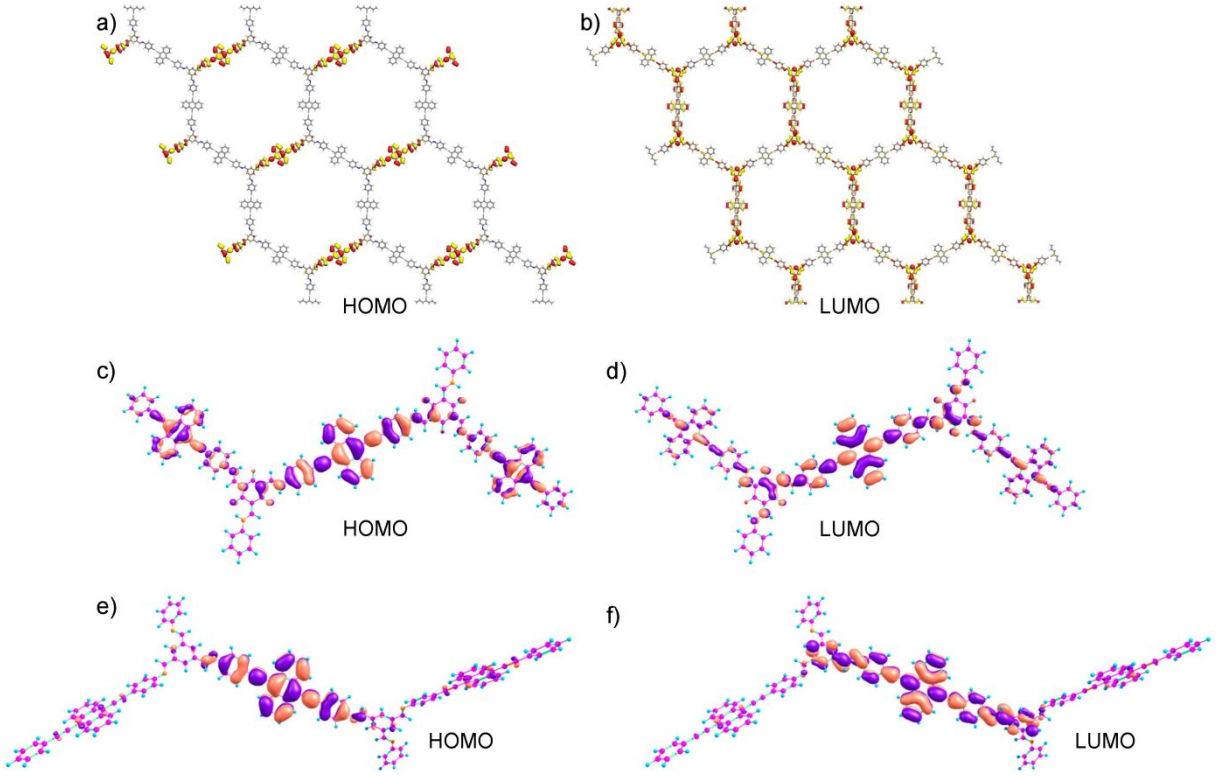

Fig. S12. The isosurface (0.015) of the electron density of a) HOMO; b) LUMO of single layer of **AntTTF**. Frontier molecular orbitals of the smallest model unit of c) and d) **AntTTH**, and e) and f) **AntTTF.**

Table S1. Calculating crystal size of **AntTTH** powder and film using Scherrer equation.

	Peak Position /2θ°	**FWHM**	**Crystallite Size** /nm	**Average Crystallite Size** /nm
AntTTH Powder	2.3	0.62	13.4	**11.7**
	3.76	0.68	12.2	
	6.52	0.8	10.4	
	7.82	0.76	10.9	
AntTTH Film	2.23	0.27	30.7	**30.0**
	3.93	0.27	30.7	
	6.02	0.29	28.7	

Table S2. Summary of electrical conductivity of reported representative COFs and compared with **AntTTH**.

COF	**Conductivity** /S cm^{-1}	**Reference**
AntTTH (Present Work)	1.2×10^{-7}	———
TTF–COF	1.2×10^{-4}	*Chem. Sci.* **2014**, *5*, 4693–4700.
1–S 1–Se 1–Te	3.7×10^{-10} 8.4×10^{-9} 1.3×10^{-7}	*Chem. Mater.* **2015**, *27*, 5487–5490.
Por–COF	4.6×10^{-11}	*CrystEngComm.* **2016**, *18*, 4259–4263.
sp^{2}C–COF	6.1×10^{-14}	*Science* **2017**, *357*, 673–676.
Lp–pi–COF	2×10^{-9}	*Langmuir* **2018**, *34*, 8731–8738.
PBHP–TAPT–COF	1.3×10^{-8}	*Nat. Commun.* **2019**, *10*, 3228.
COF–O COF–C	1×10^{-7} 2×10^{-5}	*Angew. Chem. Int. Ed.* **2019**, *58*, 16101 –16104.
COF–DC–8	2.5×10^{-5}	*J. Am. Chem. Soc.* **2019,** *141*, 11929–11937.
TANG–COF	5×10^{-12}	*J. Am. Chem. Soc.* **2020**, *142*, 2155–2160.

Table S3. DMol3 calculated valence band (E_{VB}), conduction band (E_{CB}), fermi energy level (E_F) and band gap of single and multilayer of **AntTTH** and **AntTTF**.

COF	$\boldsymbol{E_F}$ /eV	$\boldsymbol{E_{VB}}$ /eV	$\boldsymbol{E_{CB}}$ /eV	**Band gap** /eV
AntTTH_single layer	–4.059	–3.474	–4.714	1.24
AntTTH_five layers	–3.779	–3.942	–3.686	0.256
AntTTF_single layer	–4.050	–4.758	–3.343	1.415
AntTTF_five layers	–3.774	–4.013	–3.516	0.497

References:

1. Materials Studio, BIOVIA Software Inc., San Diego, CA, (2018).
2. Hourahine, B.; Aradi, B.; Blum, V.; Bonafé, F.; Buccheri, A.; Camacho, C.; Cevallos, C.; Deshaye, M. Y.; Dumitrică, T.; Dominguez, A.; Ehlert, S.; Elstner, M.; van der Heide, T.; Hermann, J.; Irle, S.; Kranz, J. J.; Köhler, C.; Kowalczyk, T.; Kubař, T.; Lee, I. S.; Lutsker, V.;

Maurer, R. J.; Min, S. K.; Mitchell, I.; Negre, C.; Niehaus, T. A.; Niklasson, A. M. N.; Page, A. J.; Pecchia, A.; Penazzi, G.; Persson, M. P.; Ř ezác, J.; Sánchez, C. G.; Sternberg, M.; Stöhr, M.; Stuckenberg, F.; Tkatchenko, A.; Yu, V. W.−z.; Frauenheim, T. DFTB+, a Software Package for Efficient Approximate Density Functional Theory based Atomistic Simulations. *J. Chem. Phys.* **2020**, *152*, 124101.

3. Gaus, M.; Cui, Q.; Elstner, M. DFTB3: Extension of the Self−Consistent−Charge Density−Functional Tight−Binding Method (SCC−DFTB). *J. Chem. Theory Comput.* **2011**, *7*, 931−948.
4. Lukose, B.; Kuc, A.; Heine, T. The Structure of Layered Covalent−Organic Frameworks. *Chem. − Eur. J.* **2011**, *17*, 2388–2392.
5. Aradi, B.; Hourahine, B.; Frauenheim, T. DFTB+, a sparse matrix−based implementation of the DFTB method, *J. Phys. Chem. A* **2007**, *111*, 5678−5684.
6. Rappe, A. K.; Casewit, C. J.; Colwell, K. S.; Goddard, W. A.; Skiff, W. M. UFF, a Full Periodic Table Force Field for Molecular Mechanics and Molecular Dynamics Simulations. *J. Am. Chem. Soc.* **1992**, *114*, 10024–10035.
7. Casewit, C. J.; Colwell, K. S.; Rappe, A. K. Application of a universal force field to organic molecules. *J. Am. Chem. Soc.* **1992**, *114*, 10035−10046.
8. Gaus, M.; Goez, A.; Elstner, M. Parametrization and Benchmark of DFTB3 for Organic Molecules. *J. Chem. Theory Comput.* **2013**, *9*, 338−354.
9. Delley, B. *J. Chem. Phys.* **1990**, *92*, 508.
10. Delley, B. *J. Chem. Phys.* **2000**, *113*, 7756.
11. Perdew, J. P.; Burke, K.; Ernzerhof, M. Generalized Gradient Approximation Made Simple. *Phys. Rev. Lett.* **1996**, *77*, 3865−3868.
12. Grimme, S. Semiempirical GGA-type density functional constructed with a long-range dispersion correction. *J. Comput. Chem.* **2006**, *27*, 1787−1799.
13. Koelling, D. D.; Harmon, B. N. A technique for relativistic spin-polarised calculations. *J. Phys. C: Solid State Phys.* **1977**, *10*, 3107.
14. Gaussian 09, Revision D.01, M. J. Frisch, G. W. Trucks, H. B. Schlegel, G. E. Scuseria, M. A. Robb, J. R. Cheeseman, G. Scalmani, V. Barone, B. Mennucci, G. A. Petersson, H. Nakatsuji, M. Caricato, X. Li, H. P. Hratchian, A. F. Izmaylov, J. Bloino, G. Zheng, J. L. Sonnenberg, M. Hada, M. Ehara, K. Toyota, R. Fukuda, J. Hasegawa, M. Ishida, T. Nakajima, Y. Honda, O. Kitao, H. Nakai, T. Vreven, J. A. Montgomery, Jr., J. E. Peralta, F. Ogliaro, M. Bearpark, J. J. Heyd, E. Brothers, K. N. Kudin, V. N. Staroverov, R. Kobayashi, J. Normand, K. Raghavachari, A. Rendell, J. C. Burant, S. S. Iyengar, J. Tomasi, M. Cossi, N. Rega, J. M. Millam, M. Klene, J. E. Knox, J. B. Cross, V. Bakken, C. Adamo, J. Jaramillo, R. Gomperts, R. E. Stratmann, O. Yazyev, A. J. Austin, R. Cammi, C. Pomelli, J. W. Ochterski, R. L. Martin, K. Morokuma, V. G. Zakrzewski, G. A. Voth, P. Salvador, J. J. Dannenberg, S. Dapprich, A. D. Daniels, Ö. Farkas, J. B. Foresman, J. V. Ortiz, J. Cioslowski, and D. J. Fox, Gaussian, Inc., Wallingford CT, 2009.